CrystEngComm

Accepted Manuscript

ROYAL SOCIETY OF CHEMISTRY

www.rsc.org/crystengcomm

Graphical abstract

Morphology-controllable Li_2SiO_3 Nanostructures

Xiaoyu Li, and Huaming Yang *

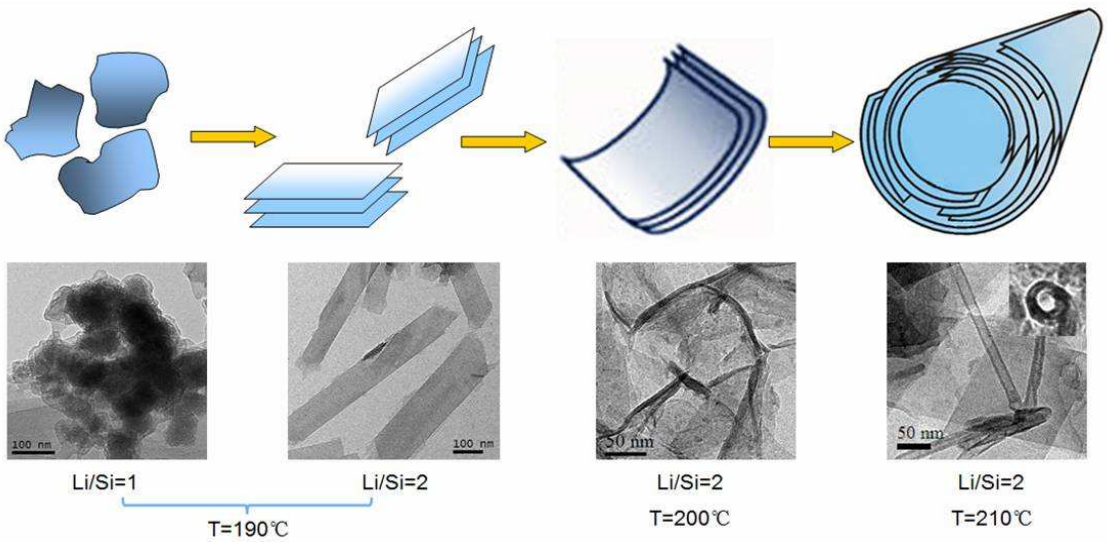

Morphology-controllable Li_2SiO_3 Nanostructures

Xiaoyu Li, and Huaming Yang*

Department of Inorganic Materials, School of Resources Processing and Bioengineering, Central South University, Changsha 410083, China

* *Corresponding author. E-mail: hmyang@csu.edu.cn, Tel.: +86-731-88830549, Fax: +86-731-88710804.*

Abstract

Hydrothermal synthesis of lithium metasilicate (Li_2SiO_3) has been systematically studied in aqueous alkaline environments by varying the Li/Si molar ratio of the solid materials and the hydrothermal temperatures. The phase structures and morphologies of the as-synthesized samples were investigated in detail by X-ray powder diffraction (XRD), transmission electron microscopy (TEM), Fourier transform infrared (FTIR) spectroscopy and N_2 porosimetry. The morphology of Li_2SiO_3 varied from nanoparticles to nanosheets and nanotubes with the reaction conditions. A Li/Si molar ratio of 2 at 190 °C was ideal for the formation of pure nanosheets with a characteristic width of 100–200 nm and a typical length of 0.2–1.5 μm. Li_2SiO_3 nanoparticles were formed at lower Li/Si molar ratio, while most of the dispersed nanosheets curled to form nanotubes at higher Li/Si molar ratio. Nanotubes were formed at 210 °C and Li/Si molar ratio of 2, which possessed a typical inner diameter of ~20 nm, outer diameter of 35 nm and a length ranged from 75 to 275 nm. Alkaline hydrothermal environment was beneficial to the formation of nanosheets and nanotubes. Atomic-level variations of the product structure from nanoparticles to nanosheets and nanotubes were depicted. Mechanism for the formation of different morphologies of Li_2SiO_3 was clarified.

Keywords: Lithium metasilicate; Nanostructures; Morphology control; Hydrothermal synthesis; Atomic-level simulation.

Introduction

Nanosheets and broad nanobelts have the trend of curling into nanorods and nanotubes[1-3]. The well-known examples could be found in the preparation of silicate[4], oxide[5, 6], hydroxide[7], sulfide[8] and noble metal nanotube[9] and so on. Metal silicates, such as $Al_2Si_2O_5(OH)_4$ (halloysite)[10-15] and $Mg_3Si_2O_5(OH)_4$ (serpentine)[16], the naturally occurring nanotubular minerals, are the most abundant and most complicated class of minerals on earth[17]. Inspired by these nanotubular minerals, in the past two decades, metal silicates possessed nanoscrolls or nanotubes structure such as $Ni_3Si_2O_5(OH)_4$[18], $Co_3Si_2O_5(OH)_4$[19] and $CuSiO_3 \cdot 2H_2O$ were artificially synthesized for promising applications, which exhibited interesting and potentially useful properties such as a high tensile strength and enhanced surface reactivity compared to the bulk materials because the properties were affected by the morphology[20]. Li_2SiO_3 are usually used as base material of painting, traditional glass[21] and ceramic raw materials[22]. In recent years, lithium silicates have been used in lithium ion batteries as solid state electrolytes, leading to all solid state batteries with improved efficiency and safety[23]. Li_2SiO_3 has also attracted significant attention as tritium breeder materials in fusion reactors[24], CO_2 captors[25] due to its special properties, such as good tritium solubility[26], high thermal stability, mechanical strength, physical and chemical stability at high temperature[27] and excellent structural compatibility with other materials. Li_2SiO_3 nanosheets or nanoscrolls should be also more promising in these applications because they possess a large specific surface area. However, there have been relatively few reports on morphology-controllable synthesis of Li_2SiO_3 in previous researches. It was clearly showed that materials possessed various morphologies exhibit very different properties[28]. New materials with special morphologies have been widely used in photocatalyst[29, 30], energy[31] and other fields[32, 33], and have promising research prospects. The width and length of the Li_2SiO_3 nanostructures will affect its physical-chemical properties, therefore, the morphology control of Li_2SiO_3 nanostructures is critically important.

In this work, we have successfully synthesized Li_2SiO_3 nanostructures in alkaline hydrothermal environment at different reaction temperatures in 24 h and reported for the first time.

The influence of controlling the hydrothermal temperature and the Li/Si molar ratio of the starting materials on the morphology and porosity of the as-obtained nanostructures was systematically studied. Furthermore, we schematically depicted the formation of different morphologies at the atomic level based on the experimental results. The controllable variation of Li_2SiO_3 nanostructures has allowed us to reflect upon the mechanism of nanostructure transformation from nanoparticles to nanosheets and nanotubes in addition to further improving the synthesis conditions of nanotubular Li_2SiO_3 towards higher yields and better control of their morphology.

Experimental

The reagents used in the experiments were analytical grade without further purification. In a typical procedure, lithium chloride ($LiCl·H_2O$) was added to 75 mL distilled water in a polypropylene beaker and stirred until all the salt had dissolved, and then added the Na_2SiO_3 aqueous solution (0.01 mol $Na_2SiO_3·9H_2O$ dissolving in 75 mL distilled water), resulting in a colorless transparent solution. The mixture was sonicated for 5 min and stirred for 90 min at room temperature. The mass of $LiCl·H_2O$ used was 0.604, 1.208 and 1.812g corresponding to a Li/Si molar ratio of 1, 2 and 3 respectively. After stirring, a quantitative mass of NaOH aqueous solution was dropped into the agitated dispersion to make an alkaline condition with continued stirring for a further 30 min, and then the solution was transferred to an autoclave and heated at 190, 200, 210 °C for 24 h. The solid products were separated from solution and washed by centrifugation with ethanol and distilled water repeatedly before drying at 80 °C.

Powder X-ray diffraction (XRD) measurements of the samples were recorded on a DX-2700 X-ray diffractometer using Cu Kα radiation (λ=0.15406 nm) at a scanning rate of 0.02 °/s with a voltage of 40 kV and 40 mA. The morphologies of Li_2SiO_3 were observed with using a transmission electron microscopy (TEM, JEOL JEM-2100F) operating at 200 kV. The as-synthesized samples for TEM analysis were dispersed in ethanol by ultrasound and a drop of each solution was deposited on a Cu grid coated by a holed carbon film and dried in air. Fourier

transform infrared (FTIR) spectra of the samples over the range of 4000-400 cm^{-1} were recorded on a Nicolet Nexus 670 FTIR spectrophotometer using KBr pellets, and the mixture was pressed into a pellet for IR measurement. The N_2 adsorption isotherms were recorded at 77 K and analyzed using an ASAP 2020 Surface Area analyzer (Micromeritics Co. Ltd.).

Results

Firstly, experiments were carried out to determine the optimum Li/Si molar ratio for nanostructures synthesis in alkaline solution whilst keeping the hydrothermal temperature at 190°C. The morphologies of the as-synthesized Li_2SiO_3 nanostructures were strongly influenced by various experimental conditions (Fig. 1), varying from nanoparticles to nanosheets and nanoscrolls at different Li/Si molar ratios. When the initial Li/Si molar ratio was designed as a value of 1, small Li_2SiO_3 nanoparticles around 100 nm were formed (Fig. 1a). When a stoichiometric ratio of Li/Si=2 was used, the Li_2SiO_3 nanosheets occurred, and was increasingly accompanied by the growth of nanoparticles (Fig. 1b). As a result, almost 100% yield of pure nanosheets with a characteristic width of 100–200 nm and a typical length of 0.2–1.5 μm were obtained. These sheets were identified by XRD (Fig. 2) and FTIR (Fig. 3) data. Upon increasing the Li/Si ratio above 2, nanosheets still occurred and most of the dispersed nanosheets exhibited obvious scrolling to form nanoscrolls, but some of them were only partially scrolled, which resulted in an irregular, conical-shaped morphology (Fig. 1c). During the hydrothermal synthesis, a strongly alkaline environment was used, and the initial concentration of alkali was crucial for the formation of nanotubes[34]. It was reported that an additional factor which could stimulate bending of nanosheets was a pronounced crystallographic mismatch in their structure which could be caused by defects[35]. Therefore, the formation of Li_2SiO_3 nanoscrolls might be attributed to the growth of nanostructures with a nonstoichiometric ratio of Li/Si under the alkaline conditions.

Fig. 2a showed the evolution of the XRD patterns of the as-synthesized Li_2SiO_3 obtained with different Li/Si molar ratios at 190°C. The reflections at 2θ of about 18.9 °, 26.9 °, 33.0 °, 38.5 °,

43.2 °, 51.7 °, 55.4 °, 59.1 °, 69.6 ° and 72.8 ° all corresponded to the crystal planes of the (020), (111), (130), (131), (221), (132), (241), (330), (133) and (332) of orthorhombic structure with space group $Cmc2_1$ (no. 36)[36]. No characteristic peaks of impurities could be detected, which indicated that pure phase of Li_2SiO_3 was successfully synthesized under the current synthetic conditions. The elemental analysis was further carried out to check the initial and real Li/Si molar ratios (Table 1), indicating that some sodium was indeed present into the samples. Because Na^+ and Li^+ have the similar ionic radius, Li^+ or Na^+ intercalation would not lead to major structural changes[37, 38]. At initial Li/Si molar ratio of 1, some sodium was present into the Li_2SiO_3 structure to stabilize it. Therefore, the XRD pattern of the samples still showed the Li_2SiO_3 phase. Additionally, the XRD peaks shift to higher values with the Li increment meant that the plane distances were being decreased (Fig. 2b&c), which may be associated with the sodium intercrystalline.

The FTIR spectra of the as-synthesized Li_2SiO_3 obtained with different Li/Si molar ratios at controlled hydrothermal temperature 190°C were recorded in Fig. 3. The characteristic bands of Li_2SiO_3 were approximately similar, while the small changes observed in some of the bands were probably associated with the rapid growth of the product. The bands between 3570–3130 and 1667 cm^{-1} were assigned to the O–H vibrations[27]. The [SiO_3^{2-}] structures group presenting in Li_2SiO_3 were of factor group symmetry *C*2*v*; therefore, seven infrared active chain stretching vibrations were expected with symmetry species $3A_1$, $3B_1$, and $1B_2$. Five of these vibrations appeared at relatively higher frequencies, and two were expected at lower frequencies[39]. The bands at 1076, 981, 935, 833, 743 cm^{-1} were attributed to the vibrations of ν_{as} Si–O–Si (A_1), ν'_{as} Si–O–Si (B_1), ν_s O–Si–O (A_1), ν_{as} O–Si–O^- (B_2) and ν_{as} Si–O–Si (B_1), respectively. The bands at 671 and 592 cm^{-1} corresponded to ν_s Si–O–Si (A_1). The bands between 530–400 cm^{-1} were due to the deformation vibrations of the terminal Si–O–(Li^+) type bonds and Li–O vibrations[40]. The bands between 530–400 and 981 cm^{-1} were increased for Li_2SiO_3 with Li/Si molar ratio of 2, which was mainly related to the continual growth of Li_2SiO_3 nanostructures and corresponding morphological transition.

Upon increasing the Li/Si ratio to 3, the decrease in intensities of these bands might be due to the obvious curling of most of Li_2SiO_3 nanosheets.

The Barrett-Joyner-Halenda (BJH) pore size distribution of the samples with different Li/Si molar ratios at 190°C was obtained using liquid nitrogen adsorption (Fig. 4), corresponding textural parameters were summarized in Table 2. According to these data, an increase in Li/Si molar ratio from 1 to 2 was also accompanied by a decrease in the volume of pores, while the Brunauer-Emmett-Teller (BET) specific surface area of Li/Si=1 sample (58.05 m^2/g) was far larger than those of two others (around 15 m^2/g). This phenomenon was associated with the reduction of number of loosely packed aggregates of nanoparticles, which would form well-shaped nanosheets. The pore volume increased again with further increasing the Li/Si molar ratio, possibly due to the occurrence of the curling structures. However, the pore sizes became more widely distributed and the mean pore size decreased.

To investigate the effect of the hydrothermal temperature on the morphology of Li_2SiO_3, the samples were collected at different hydrothermal temperatures whilst keeping the Li/Si molar ratio of 2. The TEM images showed the morphological evolution from nanosheets to nanotubes (Fig. 5). At 190°C, the typical nanosheets with regular shape were formed (Fig. 5a). Most of the nanosheets then rolled up at 200°C and they were gradually scrolled into tubular nanostructures in the different degree (Fig. 5b), which showed that increasing temperature could provide the impetus for the curling of Li_2SiO_3 nanosheets. Further increasing the hydrothermal temperature to 210°C would lead to the transformation of 2D nanosheets into 1D nanotubes with the length ranging from 75 to 275 nm (Fig. 5c). The inner and outer diameter of the nanotubes was approximately 20 nm and 35 nm, respectively. Fig. 5d clearly displayed the hollow feature of these Li_2SiO_3 nanotubes. The typical cross-section of the nanotubes was a spiral or concentric shape, indicating that the nanotubes were formed from the nanosheets under the appropriate conditions. The HRTEM image of a typical nanotube showed a multi-walled structure and an apparent spacing of 0.233 nm parallel to the tube axis (Fig. 5e). This 0.233 nm spacing was assigned to the *d*-spacing of (100) plane, suggesting that

the nanotubes were curled along the [100] direction. The XRD patterns showed that Li_2SiO_3 obtained at different temperatures with Li/Si molar ratio of 2 was the pure Li_2SiO_3 phase without other impurities (Fig. 6a). With the hydrothermal temperature increased in the reaction system, the energy required to form a curved structure increased and eventually led to the formation of nanotubes. The (111) and (131) diffractions were also slightly shifted to higher angle (Fig. 6b&c), which might be due to the rolling up of nanosheets.

The FTIR spectra of the as-synthesized Li_2SiO_3 obtained at different hydrothermal temperatures with Li/Si molar ratio of 2 was presented in Fig. 7, showing the roughly similar peak positions and band vibrations. It was indicated that the morphological change of Li_2SiO_3 nanostructures at different hydrothermal temperatures was related to the hydroxyl group (O–H) vibration bands between 3570–3130 and 1667 cm^{-1}. As the reaction temperature increased, the band corresponding to vibrations of ν'_{as} Si–O–Si (B_1) at 981 cm^{-1} decreased. So, the alkaline hydrothermal environment could provide the favourable synthesis conditions (especially the sufficient hydroxyl groups) for nanosheets and nanotubes,

Discussion

There are two major mechanisms for the formation of nanosheets and nanotubes in hydrothermal solutions, namely recrystallisation of dissolved species and exfoliation of sheets from bulk particles[41, 42]. Based on the above analysis, a possible mechanism for the formation of different Li_2SiO_3 morphologies was in detail proposed in Fig. 8, and the distance between Li lines accordingly decreased during the scrolling process (Fig. 9). Li_2SiO_3 nanostructures were varied with different Li/Si molar ratios and hydrothermal temperatures. The precipitate formed in the Li/Si=1 at 190°C showed small nanoparticles around 100 nm (Fig. 1a). Li_2SiO_3 continually grew and clearly showed the preferred growth orientation. Its morphology transformed to nanosheets when the Li ratio increased. Further increasing temperatures, a large scale of nanosheets began to curvature, and at last leading to the formation of nanotubes. It was believed that these crystals grew from solution

and acted as seeds for the formation of Li_2SiO_3 nanostructures. Actually, lithium is tetrahedrally coordinated with a mean Li–O distance of 2.0 Å, the [SiO_4] tetrahedral in Li_2SiO_3 are connected by bridge-oxygen atoms with formation of several [SiO_4] chains. [SiO_4] tetrahedra are bridged to form a chain. Each $[SiO_4]_n$ chain is surrounded by Li atoms[43]. Some researchers have stated that various nanotubes could be synthesized through rolling nanosheets into nanotubes through alkali treatment[44] .Similar process could be employed in the synthesis of Li_2SiO_3 nanotubes. After further heating, the [SiO_4] tetrahedra were arranged onto one side of the growing Li–O sheets, inorganic lamellar structure was then formed through alkali treatment based on the relatively weak hydrogen-bond and van der Waals force interactions. As a result, the Li_2SiO_3 nanoparticles transformed to nanosheets and the nanosheets curled or overlapped themselves under hydrothermal conditions to form nanotubes, the driving force for the curving of Li_2SiO_3 nanosheets was probably associated with the asymmetrical chemical environment at higher hydrothermal temperature.

Conclusions

The morphology of Li_2SiO_3 nanostructures has been effectively controlled via adjusting the hydrothermal temperature and Li/Si molar ratio. Pure nanosheets of Li_2SiO_3 with a characteristic width of 100–200 nm and a typical length of 0.2–1.5 μm were formed at a Li/Si ratio of 2 and 190°C hydrothermal temperature. With the increase of the hydrothermal temperature, the driving force for the curving of flat nanosheets was enhanced and eventually led to the formation of Li_2SiO_3 nanotubes. The products had the same crystal structure but with a different Li(I) contents at Li/Si molar ratio higher or lower than 2. Moreover, atomic-level variation of the morphology from nanoparticles to nanosheets and nanotubes was clarified, our insight into the controllable transformation of Li_2SiO_3 nanostructures from nanoparticles to nanosheets and nanotubes could be reference function to the controllable synthesis of multi-functional nanostructures. We also believe that the as-synthesized Li_2SiO_3 nanostructures could have potential application in the fields of lithium batteries, catalyst supports and ceramics.

Acknowledgements

This work was supported by the National Science Fund for Distinguished Young Scholars (51225403), Hunan Provincial Natural Science Fund for Innovative Research Groups and the Specialized Research Fund for the Doctoral Program of Higher Education (20120162110079).

References

1. R. Ma, Y. Bando, T. Sasaki, *J. Phys. Chem. B* 2004, **108**, 2115-2119.
2. D. V. Bavykin, V. N. Parmon, A. A. Lapkina and F. C. Walshc, *J. Mater. Chem.*, 2004, **14** 3370-3377.
3. M. Kitano, E. Wada, K. Nakajima, S. Hayashi, S. Miyazaki, H. Kobayashi and M. Hara, *Chem. Mater.*, 2013, **25**, 385-393.
4. Y. Kuroda, K. Ito, K. Itabashi and K. Kuroda, *Langmuir*, 2011, **27**, 2028-2035.
5. X. Chen, Y. Zhou, Q. Liu, W. Tu and Z. Zou, *CrystEngComm*, 2012, **14**, 7583-7585.
6. Z. Liang, H. Cui, K. Wang, P. Yang, L. Zhang, W. Mai, C.-X. Wang and P. Liu, *CrystEngComm*, 2012, **14**, 1723-1728.
7. D. Zheng, J. Shi, X. Lu, C. Wang, Z. Liu, C. Liang, P. Liu and Y. Tong, *CrystEngComm*, 2010, **12**, 4066-4070.
8. Z.-H. Ge, B.-P. Zhang, Z.-X. Yu and B.-B. Jiang, *CrystEngComm*, 2012, **14**, 2283-2288.
9. H. Zhu, H. Chen, J. Wang and Q. Li, *Nanoscale*, 2013, **5**, 3742-3746.
10. R. D. White, D. V. Bavykin and F. C. Walsh, *J. Phys. Chem. C*, 2012, **116**, 8824-8833.
11. A. Elshad, S. Keita, O. Ken, W. Wenbo, A. Katsuhiko and L. Yuri, *ACS Appl. Mater. Interfaces*, 2011, **3**, 4040-4046.
12. Y. Zhang, X. He, J. Ouyang and H. Yang, *Sci. Rep.*, 2013, **3**.
13. Y. Lee, G.-E. Jung, S. J. Cho, K. E. Geckeler and H. Fuchs, *Nanoscale*, 2013, **5**, 8577-8585.
14. Y. Zhang and H. Yang, *Appl. Clay Sci.*, 2012, **56**, 97-102.

15. Y. Zhang and H. Yang, *Funct. Mater. Lett.*, 2013, **06**, 1350013.

16. W. Zhu, Y. Yang, S. Hu, G. Xiang, B. Xu, J. Zhuang and X. Wang, *Inorg. Chem.*, 2012, **51**, 6020-6031.

17. H. Yang, C. Wang and Z. Su, *Chem. Mater.* , 2008, **20**, 4484-4488.

18. F. Alvarez-Ramírez, J. A. Toledo-Antonio, C. Angeles-Chavez, J. H. Guerrero-Abreo and E. López-Salinas, *J. Phys. Chem. C*, 2011, **115**, 11442-11446.

19. D. Carta, M. F. Casula, A. Corrias, A. Falqui, D. Loche, G. Mountjoy and P. Wang, *Chem. Mater.* , 2009, **21**, 945-953.

20. R. Tenne and G. Seifert, *Annu. Rev. Mater. Sci. Res.*, 2009, **39**, 387-413.

21. J. Du and L. R. Corrales, *J. Phys. Chem. B* 2006, **110**, 22346-22352.

22. A. Prasad, A. Basu and M. K. Mahata, *J. Ovonic Res.*, 2011, **7**, 61-66.

23. Y. Tomczak, K. Knapas, M. Sundberg, M. Leskelä and M. Ritala, *J. Phys. Chem. C*, 2013, **117**, 14241-14246.

24. T. Tang, Z. Zhang, J. Meng and D.-L. Luo, *Fusion Eng. Des.* , 2009, **84** 2124-2130.

25. T. L. Ávalos-Rendón and H. Pfeiffer, *Energy Fuels*, 2012, **26**, 3110-3114.

26. S. Buchner and N. M. Balzaretti, *J. Phys. Chem. Solids*, 2013, **74**, 1179-1183.

27. A. Yang, H. Wang, W. Li and J. Shi, *J. Am. Ceram. Soc.*, 2012, **95**, 1818-1821.

28. R. Mas-Ballesté, C. Gómez-Navarro, J. Gómez-Herrero and F. Zamora, *Nanoscale*, 2011, **3**, 20-30.

29. G. Zhang, Y. Gao, Y. Zhang and G. Yadan, *Environ. Sci. Technol.*, 2010, **44**, 6384-6389.

30. G. Zhang, X. Shen and Y. Yang, *J. Phys. Chem. C*, 2011, **115**, 7145-7152.

31. L. Yu, H. B. Wu and X. W. D. Lou, *Adv. Mater.*, 2013, **25**, 2296-2300.

32. X. Zhang, X. Zhang, W. Shi, X. Meng, C. Lee and S. Lee, *J. Phys. Chem. B* 2005, **109**, 18777-18780.

33. W. Zhang, M. Li, Q. Wang, G. Chen, M. Kong, Z. Yang and S. Mann, *Adv. Funct. Mater.*, 2011, **21**, 3516-3523.

34. R. D. White, D. V. Bavykin and F. C. Walsh, *J. Mater. Chem. A*, 2013, **1**, 548-556.

35. V. Petkov, P. Zavalij, S. Lutta, M. Whittingham, V. Parvanov and S. Shastri, *Phys. Rev. B*, 2004, **69**.

36. K.-F. Hesse, *Acta Cryst.*, 1977, **33**, 901-902.

37. S. Lunell, A. Stashans, L. Ojamäe, H. Lindström and A. Hagfeldt, *J. Am. Chem. Soc.* , 1997, **119**, 7374-7380.

38. V. L. Mejía-Trejo, E. Fregoso-Israel and H. Pfeiffer, *Chem. Mater.* , 2008, **20**, 7171-7176.

39. A. N. Lazarev, *Consultants Bureau*, 1972, **77-90**.

40. B. Zhang, M. Nieuwoudt and A. J. Easteal, *J. Am. Ceram. Soc.*, 2008, **91**, 1927-1932.

41. M. Wei, Y. Konishi, H. Zhou, H. Sugihara and H. Arakawa, *Solid State Commun.* , 2005, **133**, 493-497.

42. R. E. Schaak and T. E. Mallouk, *Chem. Mater.*, 2000, **12**, 3427-3434.

43. Y. Duan, H. Pfeiffer, B. Li, I. C. Romero-Ibarra, D. C. Sorescu, D. R. Luebkea and J. W. Halleyd, *Phys. Chem. Chem. Phys.*, 2013, **15**, 13538-13558.

44. W. Z. Qing Chen, G. Du, L. Peng, *Adv. Mater.*, 2002, **14**, 1208-1211.

Table 1 The elemental analysis of the as-synthesized samples at different Li/Si molar ratios.

Initial Li/Si molar ratio	Na (wt.%)	Li (wt.%)	SiO_2 (wt.%)	Final Li/Si molar ratio
1:1	0.40	9.33	59.81	1.34:1
2:1	0.17	13.31	60.34	1.89:1
3:1	0.14	14.81	61.37	2.07:1

Table 2 The textural characteristics of Li_2SiO_3 at different Li/Si molar ratios.

Li/Si molar ratio	S_{BET} (m^2/g)	V_{pores} (cm^3/g)	d_{pores}(nm)
1:1	58.05	0.12	8.47
2:1	15.39	0.04	8.27
3:1	15.09	0.10	8.22

Notes: S_{BET} = BET specific surface area, V_{pores}= total pore volume, d_{pores}= average pore diameter.

Figures captions

Fig. 1 TEM images of Li_2SiO_3 with different Li/Si molar ratios (a) 1, (b) 2 and (c) 3.

Fig. 2 (a) XRD patterns of the as-synthesized Li_2SiO_3 with different Li/Si molar ratios, (b) and (c) are the amplification of corresponding area in (a).

Fig. 3 FTIR spectra of the as-synthesized Li_2SiO_3 at different Li/Si molar ratios (a) 1, (b) 2 and (c) 3.

Fig. 4 Pore size distributions for the as-synthesized Li_2SiO_3 at different Li/Si molar ratios (a) 1, (b) 2 and (c) 3.

Fig. 5 TEM images of Li_2SiO_3 at different hydrothermal temperature: (a) 190°C, (b) 200°C and (c) 210°C, (d) TEM image of nanotubes and its open, (e) HRTEM image of Li_2SiO_3 nanotube formed at 210 °C, and a magnified image of the layer structure of the wall with orientation of the crystal planes is shown in the insets.

Fig. 6 (a) XRD patterns of Li_2SiO_3 at different hydrothermal temperature, (b) and (c) are the amplification of corresponding area in (a).

Fig. 7 FTIR spectra of Li_2SiO_3 at different hydrothermal temperatures.

Fig. 8 Proposed mechanism for the morphology control of Li_2SiO_3.

Fig. 9 Atomic structures of Li_2SiO_3 synthesized at different hydrothermal temperatures. The distance between Li lines decreases during the curling process.

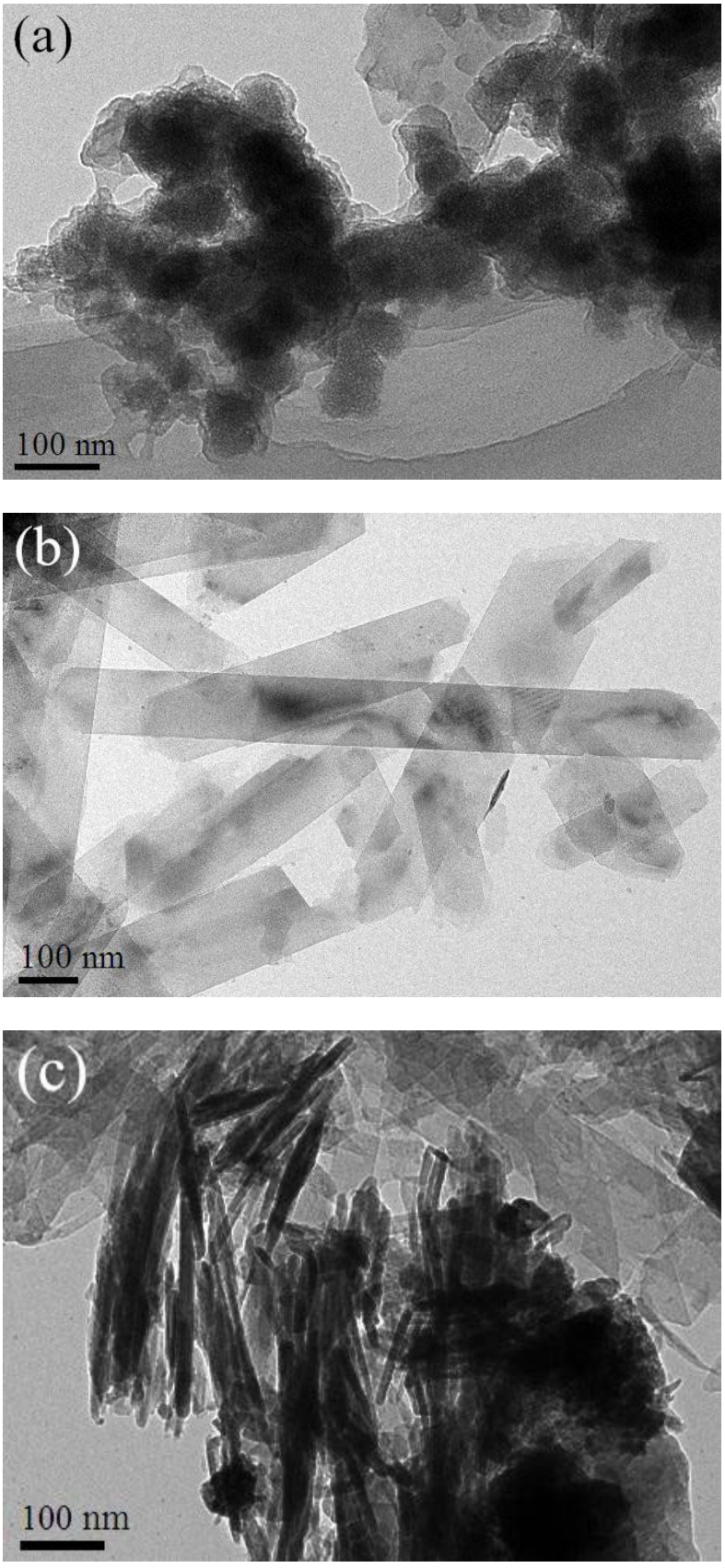

Fig. 1 TEM images of Li_2SiO_3 with different Li/Si molar ratios (a) 1, (b) 2 and (c) 3.

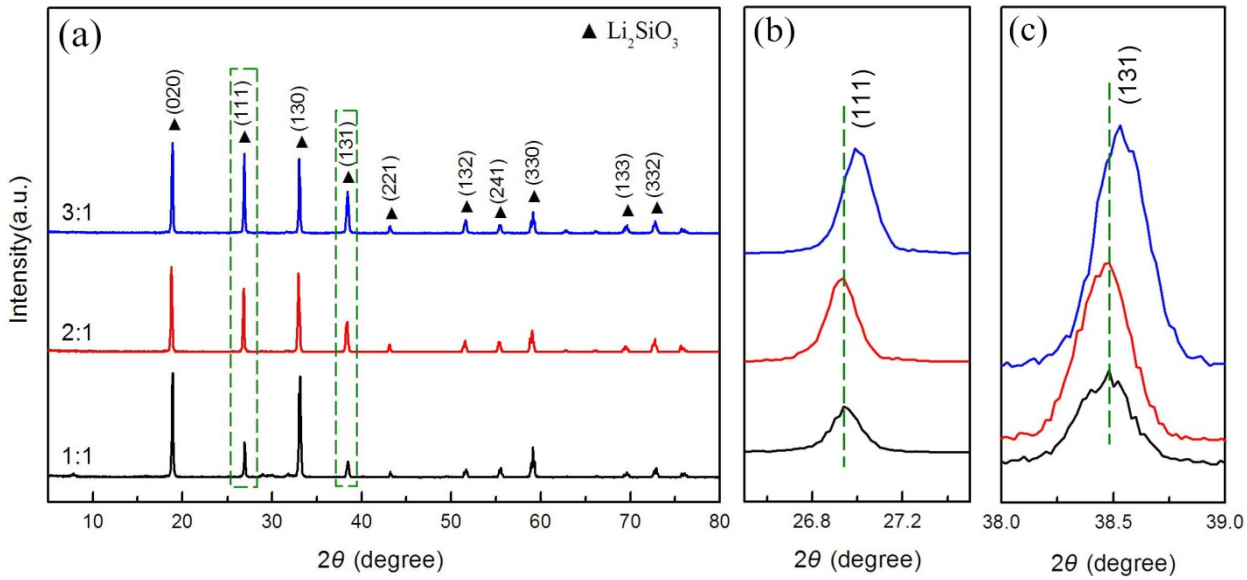

Fig. 2 (a) XRD patterns of the as-synthesized Li_2SiO_3 with different Li/Si molar ratios, (b) and (c) are the amplification of corresponding area in (a).

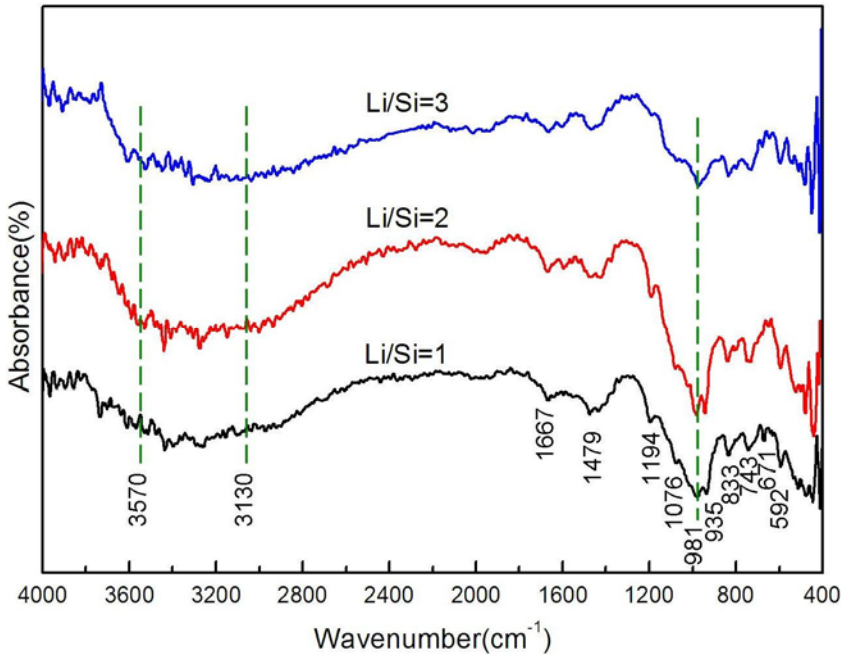

Fig. 3 FTIR spectra of the as-synthesized Li_2SiO_3 at different Li/Si molar ratios (a) 1, (b) 2 and (c) 3.

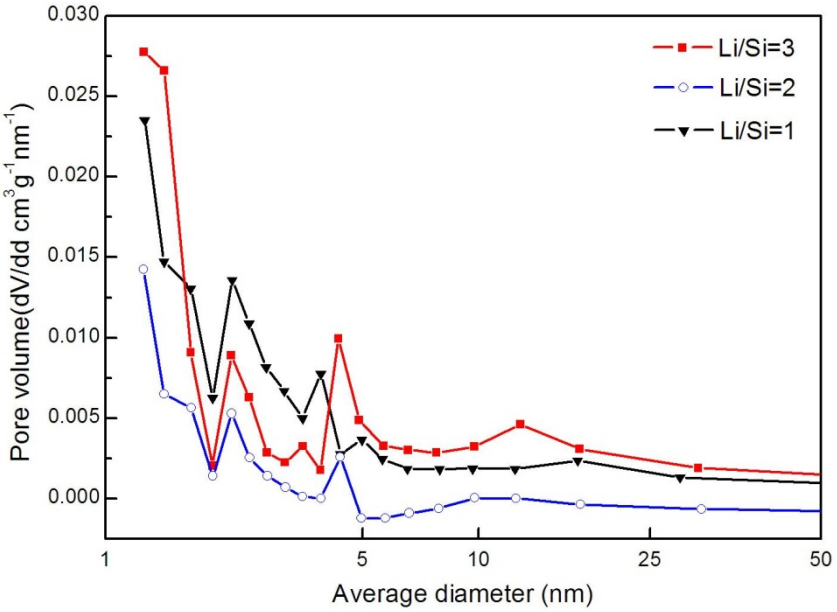

Fig. 4 Pore size distributions for the as-synthesized Li_2SiO_3 at different Li/Si molar ratios (a) 1, (b) 2 and (c) 3.

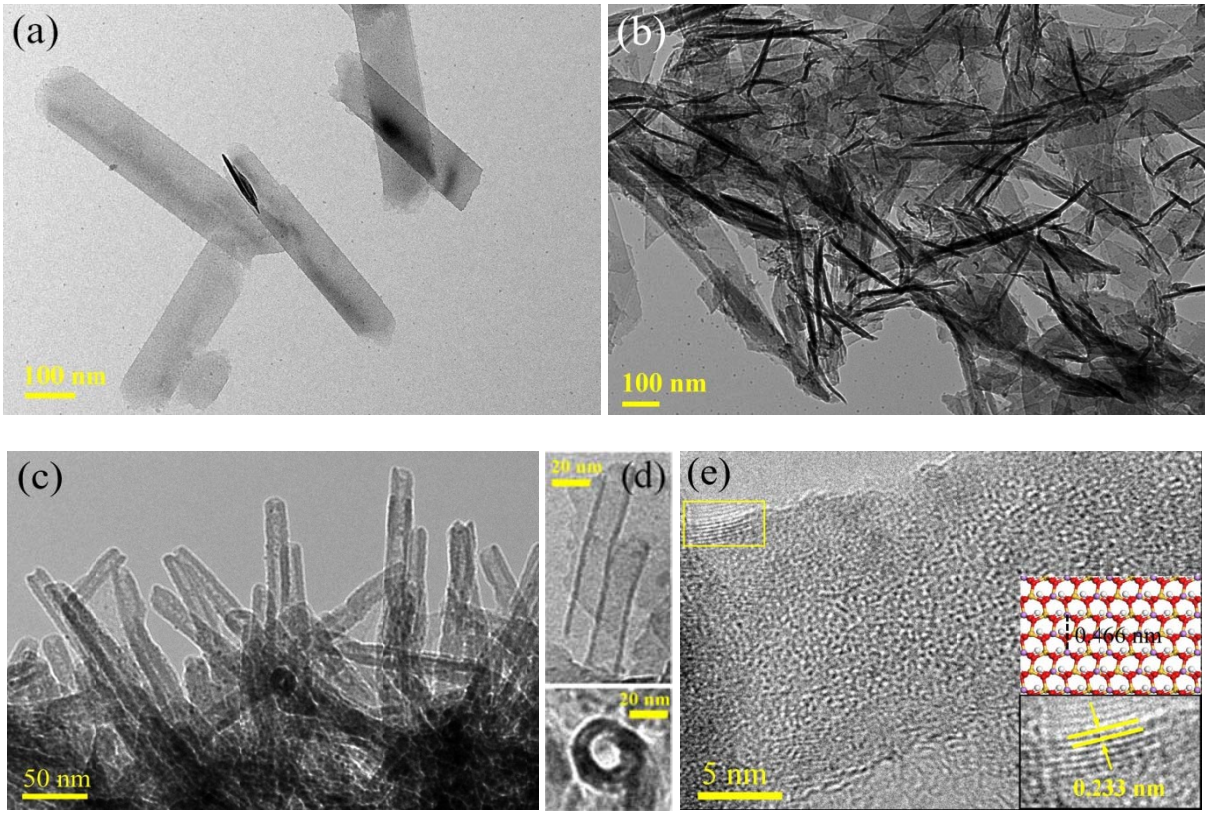

Fig. 5 TEM images of Li_2SiO_3 at different hydrothermal temperature: (a) 190°C, (b) 200°C and (c) 210°C, (d) TEM image of nanotubes and its open, (e) HRTEM image of Li_2SiO_3 nanotube formed at 210 °C, and a magnified image of the layer structure of the wall with orientation of the crystal planes is shown in the insets.

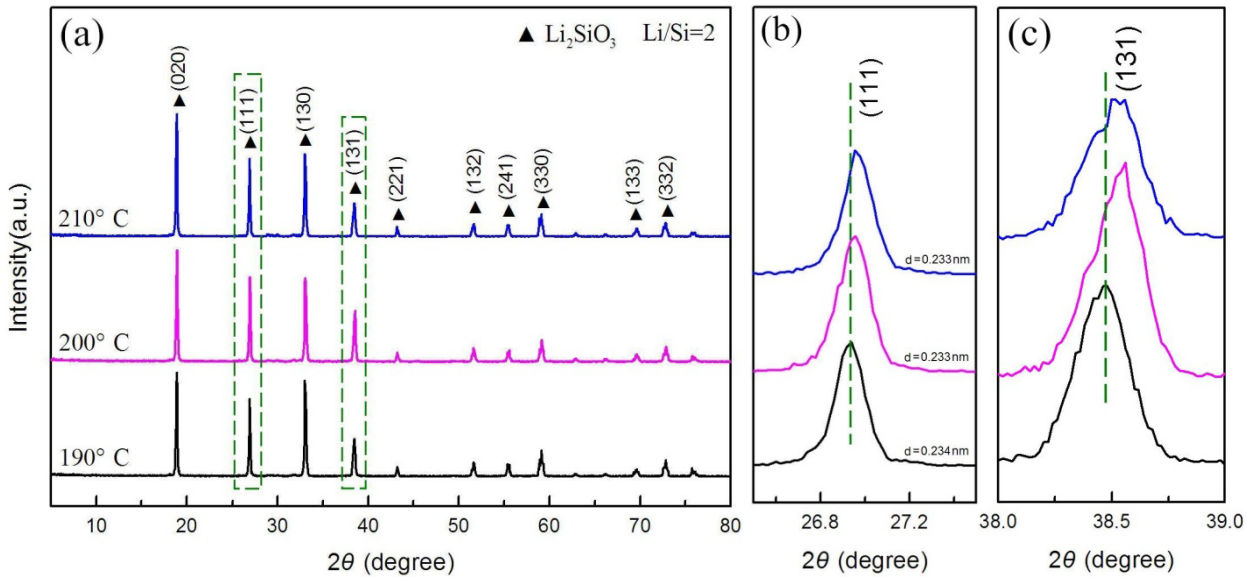

Fig. 6 (a) XRD patterns of Li_2SiO_3 at different hydrothermal temperature, (b) and (c) are the amplification of corresponding area in (a).

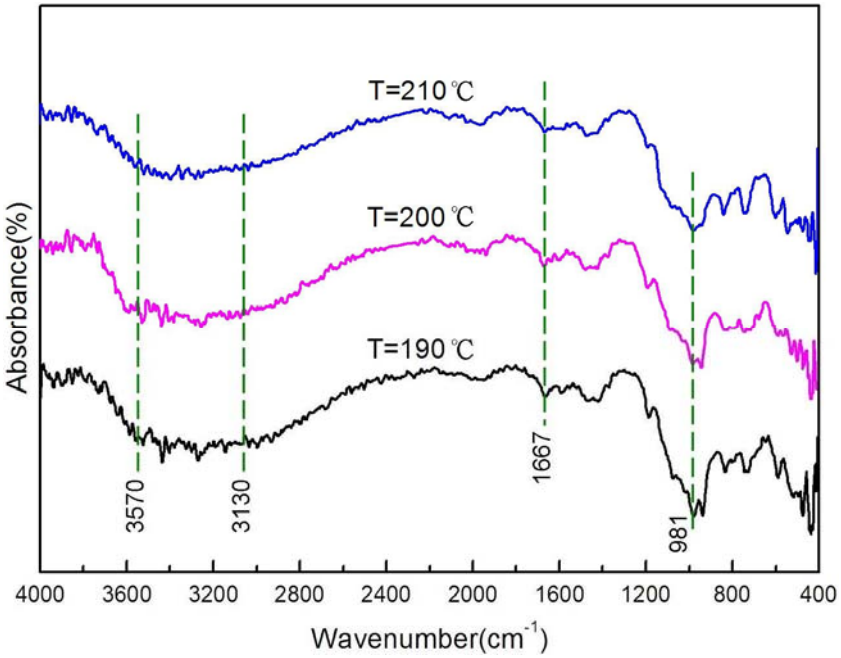

Fig. 7 FTIR spectra of Li_2SiO_3 at different hydrothermal temperatures.

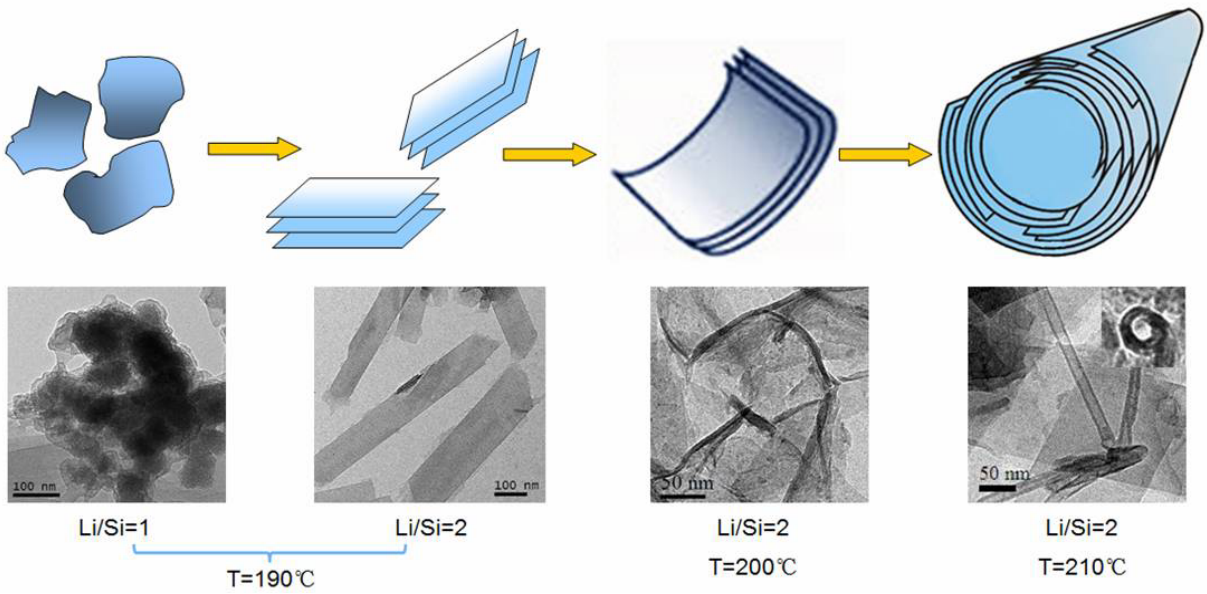

Fig. 8 Proposed mechanism for the morphology control of Li_2SiO_3.

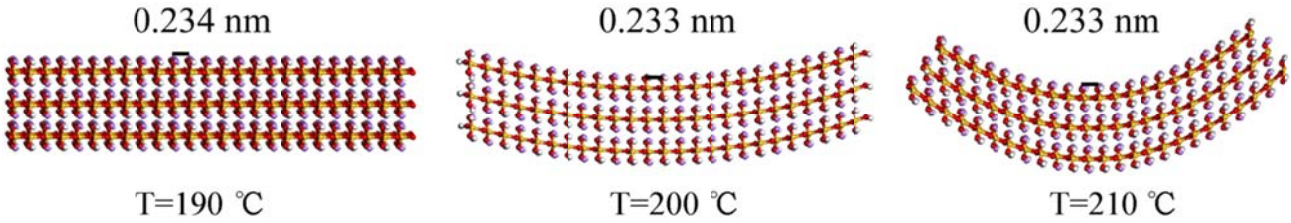

Fig. 9 Atomic structures of Li_2SiO_3 synthesized at different hydrothermal temperatures. The distance between Li lines decreases during the curling process.